Mineralogical Magazine (2022), **86**, 929–939
doi:10.1180/mgm.2022.103

CAMBRIDGE UNIVERSITY PRESS

Article

Minerals of the arctite supergroup from the Bellerberg volcano xenoliths, Germany

Rafał Juroszek[1]*, Biljana Krüger[2], Beata Marciniak-Maliszewska[3] and Bernd Ternes[4]

[1]Institute of Earth Sciences, Faculty of Natural Sciences, University of Silesia, Będzińska 60, 41-205 Sosnowiec, Poland; [2]Institute of Mineralogy and Petrography, University of Innsbruck, Innrain 52, 6020 Innsbruck, Austria; [3]Faculty of Geology, University of Warsaw, Żwirki and Wigury 93, 02-089 Warsaw, Poland; and [4]Retired, Mayen, Germany

Abstract

The recently defined arctite supergroup contains nine mineral members defined as hexagonal intercalated antiperovskites, most of which have been found in pyrometamorphic rocks of the Hatrurim Complex, Israel. Three members of this supergroup: nabimusaite, gazeevite and zadovite, were identified for the first time in altered carbonate–silicate xenoliths from the Caspar and Scherer quarries, Bellerberg volcano in Germany. Present work focuses on the chemical, structural and spectroscopic investigation of these minerals and their correlation with holotype counterparts. The apparent differences are mainly related to the chemical composition, types of substitution in the tetrahedral and antiperovskite layers within the crystal structure, and position of bands in the Raman spectra. In the Bellerberg volcano xenoliths, the crystallisation of nabimusaite and gazeevite is caused by high-temperature alteration of early mineral associations (clinker-like phases) and their reaction with melt or gas generated by volcanic activity. In turn, the formation of zadovite is related to the Ba-rich silicate melt that filled the intergranular space between the rock-forming minerals.

Keywords: arctite supergroup, nabimusaite, gazeevite, zadovite, Bellerberg volcano, Germany

(Received 29 June 2022; accepted 16 August 2022; Accepted Manuscript published online: 26 August 2022; Associate Editor: Peter Leverett)

Introduction

The minerals of the arctite supergroup belong to the hexagonal intercalated antiperovskites featured by the anion-centred octahedra units in its structure (Galuskin *et al.*, 2021). Nowadays, this supergroup contains nine members, which, based on the antiperovskite and tetrahedral layers arrangement, are divided into the zadovite and arctite groups and one ungrouped member – aravaite, $Ba_2Ca_{18}[(SiO_4)_6(PO_4)_3(CO_3)]F_3O$ (Krüger *et al.*, 2018; Galuskin *et al.*, 2021). Zadovite, $BaCa_6[(SiO_4)(PO_4)](PO_4)_2F$ (Galuskin *et al.*, 2015b), aradite, $BaCa_6[(SiO_4)(VO_4)](VO_4)_2F$ (Galuskin *et al.*, 2015b), gazeevite, $BaCa_6(SiO_4)_2(SO_4)_2O$ (Galuskin *et al.*, 2017) and stracherite, $BaCa_6(SiO_4)_2[(PO_4)(CO_3)]F$ (Galuskin *et al.*, 2018b) represent the zadovite structural type (*TA*) characterised by intercalation of tetrahedral (*T*) and single antiperovskite layers (*A*). In turn, arctite, $Ba(Ca_7Na_5)(PO_4)_4(PO_4)_2F_3$ (Khomyakov *et al.*, 1983; Sokolova *et al.*, 1984), nabimusaite, $KCa_{12}(SiO_4)_4(SO_4)_2O_2F$ (Galuskin *et al.*, 2015a), dargaite, $BaCa_{12}(SiO_4)_4(SO_4)_2O_3$ (Galuskina *et al.*, 2019) and ariegilatite, $BaCa_{12}(SiO_4)_4(PO_4)_2OF_2$ (Galuskin *et al.*, 2018a) belong to the arctite structural type (TA^3) described by intercalation of the tetrahedral (*T*) and triple antiperovskite layers (A^3). The ungrouped aravaite ($TATA^3$ structural type) is different and consists of blocks formed by the intercalation of zadovite and arctite structural modules (Krüger *et al.*, 2018; Galuskin *et al.*, 2021).

With the exception of arctite, all supergroup members have been found in unique high-temperature pyrometamorphic rocks of the Hatrurim Complex distributed along the Dead Sea Rift of Israel, West Bank (Palestinian Autonomy), and Jordanian territories (Sokol *et al.*, 2020; Galuskin *et al.*, 2021). Arctite was discovered in pegmatite veins in nepheline syenite at the Vuonnemiok River, Khibiny Massif, Kola Peninsula, Russia (Khomyakov *et al.*, 1983). Some dargaite and gazeevite occurrences have been reported from the altered carbonate–silicate xenoliths within rhyodacites of the Shadil-Khoch volcano, Graeter Caucasus (Galuskin *et al.*, 2017).

In the present paper, we report a new occurrence for the three arctite-supergroup minerals, nabimusaite, gazeevite and zadovite: the Bellerberg volcano, Eifel district, Rhineland-Palatinate, Germany. We present chemical, spectroscopic, and structural data for these minerals and compare our results with the data reported for their holotype counterparts.

Occurrence, general appearance and mineral association

Geological settings

The Bellerberg volcano, worked as an active quarry, is characterised by the presence of various thermally metamorphosed carbonate–silicate and silicate xenoliths within basaltic lava. The locality belongs to the quaternary volcano region in the Eastern Eifel, Rhineland-Palatinate, Germany (Hentschel, 1987; Mihajlovic *et al.*, 2004). The wide variety of xenoliths occurring in the volcanic rocks of the Bellerberg volcano area is due to metamorphic transformation and a different protolith composition

*Author for correspondence: Rafał Juroszek, Email: rafal.juroszek@us.edu.pl
Cite this article: Juroszek R., Krüger B., Marciniak-Maliszewska B. and Ternes B. (2022) Minerals of the arctite supergroup from the Bellerberg volcano xenoliths, Germany. *Mineralogical Magazine* **86**, 929–939. https://doi.org/10.1180/mgm.2022.103

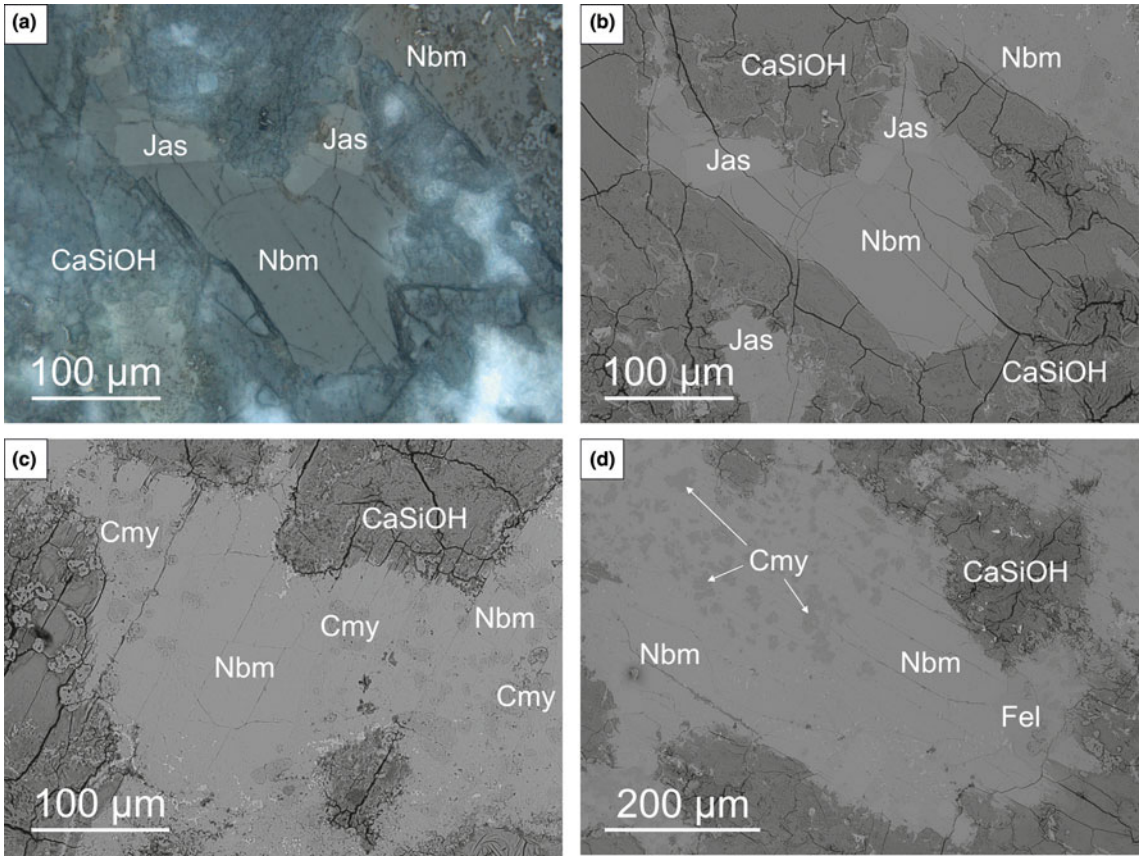

Fig. 1. Optical (a) and BSE (back-scattered electron) images (b–d) of nabimusaite and associated minerals in the carbonate–silicate xenoliths. Euhedral homogenous nabimusaite crystals with visible parting/cleavage (a–b) and nabimusaite crystals containing chlormayenite inclusions (c–d); CaSiOH – hydrated Ca-silicates; Cmy – chlormayenite; Fel – fluorellestadite; Jas – jasmundite; Nbm – nabimusaite. Sample #11.

(Hentschel, 1987; Mihajlovic *et al.*, 2004; Juroszek *et al.*, 2018). The starting material could be from any of the host rocks that were penetrated and carried away by the erupting. These include: volcanic rocks of earlier eruptions of more or less different compositions; Devonian and younger sedimentary rocks, such as clays, slates, greywacke, sandstone, quartzite, and lime- to marlstones; rocks from the deeper areas of the Earth crust; or fragments of the Earth's mantle (Hentschel, 1987). The presence of characteristic mineral assemblages indicate that, to a greater or lesser extent, xenoliths are transformed by surrounding magma, and mineral phases were formed due to metamorphism at very high-temperature conditions. The differences in the degree of conversion can be caused by many factors, such as: various temperatures of the magma; different cooling rates; different levels of water vapour and other volatile substances (fluorine, chlorine and sulfur); different sizes of xenoliths; and multiple heating of xenoliths and/or prolonged exposure to escaping hot gases or by lava entering the environment (Hentschel, 1987). Moreover, the xenoliths from Bellerberg volcano are known for their diversity of secondary, low-temperature phases and the source of several new mineral species (Abraham *et al.*, 1983; Irran *et al.*, 1997; Mihajlovic *et al.*, 2004; Chukanov *et al.*, 2012, 2015; Galuskin *et al.*, 2016; Juroszek *et al.*, 2018).

Xenolith samples presented in this study were collected by Bernd Ternes from the Caspar and Scherer quarries in the Bellerberg volcano area.

Nabimusaite

Nabimusaite forms colourless subhedral crystals with a characteristic parting/cleavage along (001) (Fig. 1). The nabimusaite crystal size usually exceeds 100 µm, but the biggest ones reach ~500 µm. It was observed that some crystals are homogeneous (Fig. 1a,b), whereas others contain chlormayenite inclusions (Fig. 1c,d).

In an analysed xenolith sample from Caspar quarry (50.35°N, 7.23°E), nabimusaite is a rock-forming mineral associated with the fluorapatite–fluorellestadite mineral series, jasmundite, larnite and ternesite (Fig. 1). Chlormayenite, occurring mainly as inclusions in nabimusaite crystals (Fig. 1c,d), minerals of the sharyginite–shulamitite series, brownmillerite, lakargiite and vapnikite are less common accessory phases. Most of the minerals mentioned are surrounded by secondary, low-temperature phases represented by various undiagnosed hydrated Ca-silicates, minerals of the ettringite–thaumasite series, and hydrocalumite. Periclase and Sr-bearing baryte are very rare.

Gazeevite

Gazeevite is an accessory mineral found in a xenolith sample from Scherer quarry (50.35°N, 7.24°E), which forms poikilitic anhedral and subhedral crystals ~50–150 µm in size (Fig. 2a–c). Usually, gazeevite crystals are embedded in the larnite matrix and overgrow and intergrow with fluorapatite–fluorellestadite individuals

https://doi.org/10.1180/mgm.2022.103 Published online by Cambridge University Press

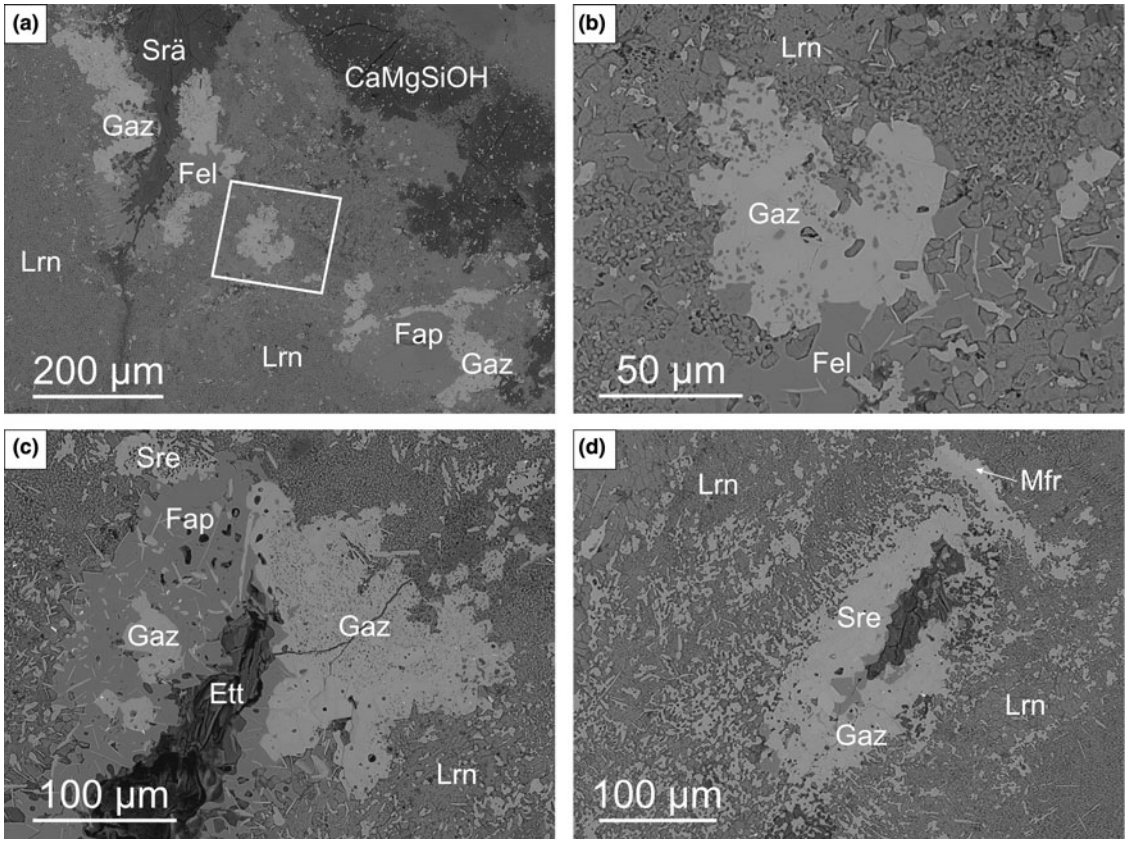

Fig. 2. The fragment of carbonate–silicate xenolith with gazeevite and associated minerals (a). The framed area magnified in b shows gazeevite crystals in the coarse-grained larnite matrix. Overgrows and intergrows of gazeevite crystals with fluorapatite–fluorellestadite (a–c), as well as with magnesioferrite and srebrodolskite grains (d); BSE images; CaMgSiOH – hydrated Ca-Mg-silicates; Ett – ettringite; Fap – fluorapatite; Fel – fluorellestadite; Gaz – gazeevite; Lrn – larnite; Mfr – magnesioferrite; Sre – srebrodolskite; Srä – strätlingite. Sample #EF15-3.

(Fig. 2a–c). Some gazeevite overgrown by magnesioferrite and srebrodolskite was also observed (Fig. 2d).

A group of gazeevite crystals was detected in the part of the xenolith near the contact zone with basaltic rock. The xenolith consists of high-temperature rock-forming minerals such as wollastonite, larnite, minerals of the gehlenite–alumoåkermanite–åkermanite, fluorapatite–fluorellestadite and brownmillerite–srebrodolskite series. In turn, the basaltic rock includes mainly K-feldspar, titanite, and minerals of the diopside–hedenbergite series. Occasionally, single quartz crystals were also noted. Garnets of the andradite–schorlomite–kerimasite series, perovskite, magnesioferrite, hematite, zircon, calzirtite and baddeleyite were recognised as accessory phases in the altered basaltic rock. Low-temperature secondary mineralisation is widespread in the sample studied and represented by ettringite, various hydrated Ca–Mg-silicates and Ca-aluminosilicates such as tobermorite, tacharanite, afwillite, strätlingite, hydrocalumite, and minerals of the zeolite group such as flörkeite and chabazite.

Zadovite

Zadovite is the rarest arctite-supergroup mineral and is described in xenoliths from the Caspar quarry for the first time. It forms tiny colourless subhedral and anhedral crystals reaching ~15–40 μm in size (Fig. 3). Usually, zadovite crystals are scattered in individual veinlets of an aluminosilicate matrix, composed of rock-forming phases, mainly wollastonite and gehlenite, which indicates signs of initial alteration, and some hydrated Ca-silicates (Fig. 3).

The xenolith fragment in which zadovite was identified is characterised by secondary alteration and the dominance of low-temperature mineral assemblages. The rock-forming minerals are mainly high-temperature phases such as wollastonite, larnite, gehlenite, nepheline and magnesioferrite. Kalsilite, bredigite, chlormayenite, fluorapatite, srebrodolskite, perovskite, hematite, minerals of the sharyginite–shulamitite series, alumoåkermanite and Sr-, Fe^{2+}-bearing melilite-group minerals are less abundant than rock-forming phases. The xenolith specimen also contains various Zr minerals, such as zircon, wadeite, lakargiite, calzirtite and baddeleyite. Zadovite, together with walstromite, fresnoite, bennesherite, celsian and mazorite, form the unique Ba-mineralisation. Secondary phases are represented by various hydrated Ca-silicates and aluminosilicates such as tobermorite, jennite, afwillite and hydrocalumite, minerals of ettringite–thaumasite series, calcite, baryte, Sr-bearing baryte, and some zeolites.

Materials and methods of investigation

The preliminary chemical composition and crystal morphology of the arctite-supergroup minerals, as well as associated phases from the Bellerberg volcano xenoliths, were carried out using an analytical Phenom XL scanning electron microscope, which is equipped with an EDS (energy-dispersive X-ray spectroscopy) detector (Institute of Earth Sciences, Faculty of Natural Sciences, University of Silesia, Sosnowiec, Poland).

Electron microprobe analyses (EMPA) of nabimusaite, gazeevite, zadovite and associated minerals were performed

https://doi.org/10.1180/mgm.2022.103 Published online by Cambridge University Press

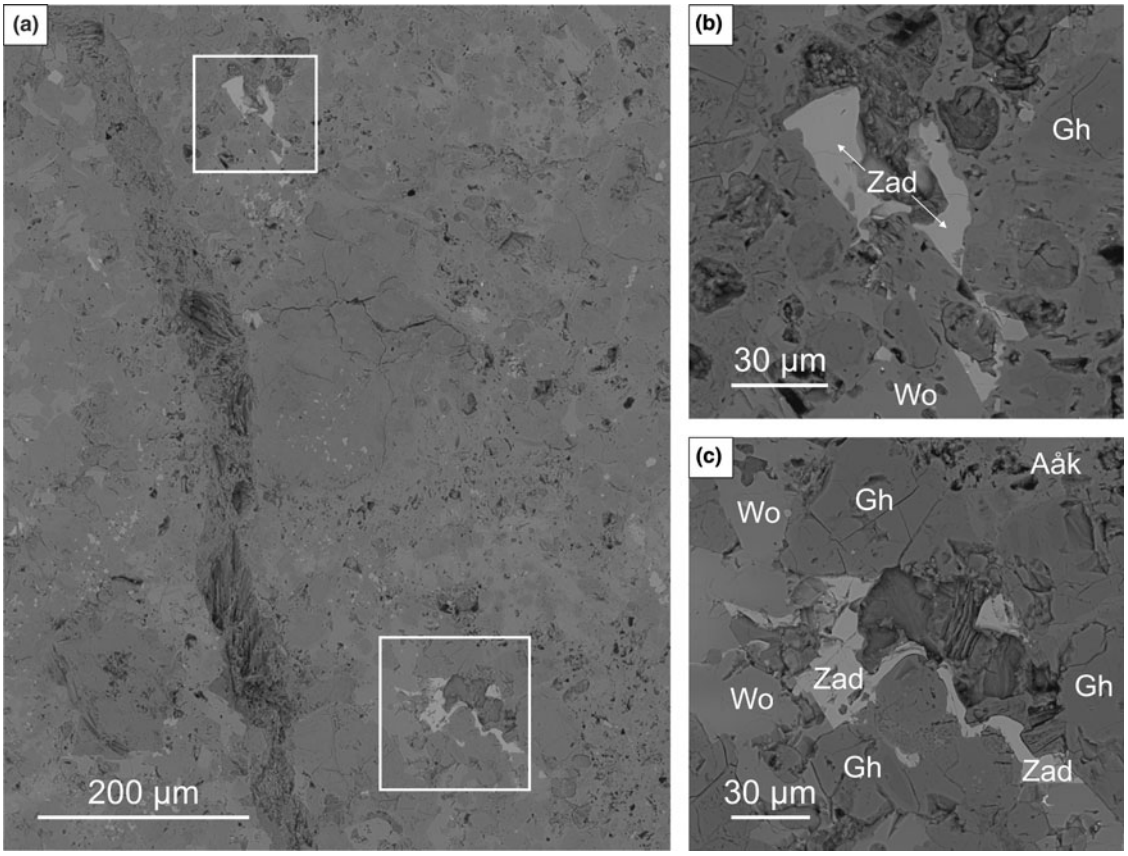

Fig. 3. Partially altered xenolith fragment composed mainly of wollastonite and gehlenite–alumoåkermanite series minerals (a). The framed sections are magnified in (b) and (c) and show zadovite crystals; BSE images; Aåk – alumoåkermanite; Gh – gehlenite; Wo – wollastonite; Zad – zadovite. Sample #15.

on CAMECA SX100 apparatus at 15 kV acceleration voltage and 10–20 nA beam current (Faculty of Geology, University of Warsaw, Poland). The following lines (and standards) were used during the measurements: Ba*L*α and S*K*α (baryte); P*K*α (YPO_4 and Apat_BB); Ca*K*α and Si*K*α (diopside); Al*K*α and K*K*α (orthoclase); Ti*K*α (rutile); Na*K*α (albite), Sr*L*α (celestine); Fe*K*α (Fe_2O_3); V*K*α (V_2O_5); and F*K*α (synthetic fluorophlogopite). Due to the size and character of the crystals, the beam diameter differed for each arctite-supergroup member: 10 µm for nabimusaite, 3 µm for gazeevite and ~1 µm for zadovite.

The Raman spectra of nabimusaite, gazeevite and zadovite were recorded on a WITec alpha 300R Confocal Raman Microscope (Institute of Earth Sciences, Faculty of Natural Sciences, University of Silesia, Sosnowiec, Poland) equipped with an air-cooled solid laser 633 nm and a CCD (closed-circuit display) camera operating at –61°C. The laser radiation was coupled to a microscope through a single-mode optical fibre with a diameter of 50 µm. An air Zeiss (LD EC Epiplan-Neofluan DIC–100/0.75NA) objective was used. The scattered light was focused on multi-mode fibre (100 µm diameter) and a monochromator with a 600 mm^{-1} grating. Raman spectra were accumulated by 15 scans with an integration time of 10 s; resolution was 3 cm^{-1}. The monochromator was calibrated using the Raman scattering line of a silicon plate (520.7 cm^{-1}). All spectra were processed using the Spectracalc software package *GRAMS*. The Raman bands were fitted using a Gauss–Lorentz cross-product function with the minimum number of component bands used for the fitting process.

Single-crystal X-ray studies were carried out with synchrotron radiation. The diffraction measurements were performed at the X06DA beamline of the Swiss Light Source (Paul Scherrer Institute, Villigen, Switzerland). The experiments were done at ambient conditions with the wavelength tuned to 0.70848 Å, and a multi-axis PRIGo goniometer was used to position and rotate the crystals. The X-ray diffraction data were collected with a Pilatus-2M-F detector, which was placed at a distance of 90 mm from the crystals and vertically translated by 55 mm off-centre to increase the resolution of the data. A total of 3600 frames were recorded using a fine-sliced (0.1) ω-scan at 0.1 seconds per frame. Lattice parameters and data reduction were made using *CrysAlisPro*. The crystal structure refinement was performed with *Jana2006* (Petříček *et al.*, 2014). The further details of the intensity data and crystal-structure refinements of nabimusaite, gazeevite and zadovite are summarised in Table 1. Information about final atomic coordinates, anisotropic displacement parameters, or selected bond lengths are listed in the crystallographic information files, deposited with the Principal Editor of *Mineralogical Magazine* and available as Supplementary material (see below).

Results

Chemical data

Results of the electron microprobe analyses of nabimusaite, gazeevite and zadovite from the Caspar and Scherer quarries are presented in Table 2. The empirical formula of nabimusaite calculated on the basis of 27 (O+F) anions is as follows:

https://doi.org/10.1180/mgm.2022.103 Published online by Cambridge University Press

$(K_{0.79}Sr_{0.10}Ca_{0.04}Ba_{0.02})_{\Sigma 0.95}(Ca_{11.94}Na_{0.06})_{\Sigma 12.00}[(Si_{3.80}Al_{0.10}S_{0.06}Ti_{0.02}Fe_{0.02})_{\Sigma 4.00}O_{16.00}][(S_{1.96}P_{0.04})_{\Sigma 2.00}O_{8.00}]O_2(F_{0.93}O_{0.07})_{\Sigma 1.00}$. The latter empirical formula of nabimusaite is close to the end-member formula, $KCa_{12}(SiO_4)_4(SO_4)_2O_2F$, with the end-member content equal to 83%.

The empirical formula of gazeevite, calculated on 17 (O+F) anions, is as follows: $(Ba_{0.86}Sr_{0.05}K_{0.05}Ca_{0.04})_{\Sigma 1.00}(Ca_{6.00}Na_{0.03})_{\Sigma 6.03}[(Si_{1.97}Al_{0.02}Fe_{0.01})_{2.00}O_{8.00}][(S_{1.71}P_{0.17}Si_{0.06}V_{0.05})_{\Sigma 1.96}O_{8.00}](O_{0.53}F_{0.34})_{\Sigma 0.87}$, with a simplified formula of $BaCa_6(SiO_4)_2(SO_4)_2(O,F)$.

The crystal-chemical formula of zadovite calculated on 17 (O+F) anions is as follows: $(Ba_{0.99}Sr_{0.03})_{\Sigma 1.02}(Ca_{5.96}Na_{0.05})_{\Sigma 6.01}[(Si_{1.31}P_{0.69})_{\Sigma 2.00}O_{8.00}][(P_{1.53}S_{0.36}V_{0.10}Fe_{0.01})_{\Sigma 2.00}O_{8.00}]F_{1.01}$, and the end-member formula is $BaCa_6[(SiO_4)(PO_4)](PO_4)_2F$ (Galuskin *et al.*, 2015b). The increased Si and considerable S (0.36 atoms per formula unit (apfu)) contents with a simultaneous decrease of P content at both tetrahedral positions of the analysed sample (Table 2) confirms the $Si^{4+}+S^{6+}\leftrightarrow 2P/V^{5+}$ substitution scheme characteristic for the zadovite-group minerals (Galuskin *et al.*, 2015b).

Crystal structure data

Nabimusaite belongs to the arctite structural type (TA^3), characterised by the intercalation of single tetrahedral (T) and triple antiperovskite layers (A^3) (Fig. 4a). The intercalated tetrahedral layers consist of large K cations and $(SO_4)^{2-}$ tetrahedra (Fig. 4b). The K site in the nabimusaite structure is partly occupied by Ba, which was also reported in the previous description (Galuskin *et al.*, 2015a). Potassium cation is coordinated by twelve oxygen atoms (6 × O1 and 6 × O3) with the average bond distances K–O1 = 2.9111 Å and K–O3 = 3.3703 Å. In the SO_4-tetrahedron, there are three shorter S–O1 = 1.4697(9) Å and one longer S–O4 = 1.4864(18) Å bond lengths, with <S–O> = 1.4739 Å. Each of the O1 atoms at the base of the SO_4 tetrahedron bonds to K and Ca1 atoms in the antiperovskite layers. The apical O4 atom of a S-tetrahedron is also bonded to the Ca1 atom.

Along z, the antiperovskite layers in the nabimusaite structure form linear face-sharing triplets of anion-centred octahedra (Fig. 4a). Two SiO_4 tetrahedra with the up and down sequence occur between these octahedral triplets (Fig. 4c). In the centre of antiperovskite layers, the $(O8)^{2-}$ anion is octahedrally coordinated by six Ca2 atoms, with the O8–Ca2 bond length of 2.3342(2) Å. Two adjacent octahedra of the triplets are occupied simultaneously by F^- and O^{2-} anions and coordinated by three Ca2 atoms, due to the shared face with $O8Ca2_6$ octahedra, and three Ca1 atoms. The bond length equals 2.4411(10) Å for O7–Ca2 and 2.3889(9) Å for O7–Ca1, respectively. According to the chemical composition, additional impurities at the Si sites are insignificant ~0.2 apfu, which should not affect the bond lengths. The average Si–O bond lengths for Si1 and Si2 tetrahedra are 1.639 Å and 1.630 Å, respectively. The Si1 tetrahedra share three O2 with the Ca2 atoms, whereas the apical O5 is linked only to Ca1. In turn, the apical O6 of Si2 tetrahedra is also bonded to the Ca2 atoms, while three O3 are joined to Ca1 and Ca2.

Gazeevite and zadovite represent the same structural type. Their structures are characterised by the alternation of single tetrahedral (T) and single antiperovskite layers (A) (Fig. 5). The main differences between these two related structures are observed in the diverse occupation at the $T1$ and $T2$ sites located at the three-fold inversion axis and different anion-centred octahedra in the antiperovskite layers (Fig. 5).

The tetrahedral Ba-bearing layers in the gazeevite structure have the following composition $Ba(SO_4)_2$. Each large Ba atom coordinated by 6+6 oxygen atoms with 6 × 2.876(3) Å (Ba–O3) and 6 × 3.245(3) Å (Ba–O2) bonds is linked to six tetrahedra (Fig. 5b). The EMPA also confirmed a minor K amount (~8%)

Table 1. Parameters for X-ray data collection and crystal-structure refinement for nabimusaite, gazeevite and zadovite.

Mineral	Nabimusaite	Gazeevite	Zadovite
Refined chemical formula	$K_{0.964}Ba_{0.036}Ca_{12.00}Si_{4.00}S_{2.00}O_{26}F_{1.00}$	$K_{0.083}Ba_{0.917}Ca_{6.00}Si_{2.00}S_{2.00}O_{17}$	$Ba_{1.00}Ca_{6.00}Si_{2.00}P_{2.00}O_{16}F_{1.00}$
Space group	$R\bar{3}m$	$R\bar{3}m$	$R\bar{3}m$
Cell parameters	$a = b = 7.19660(10)$ Å; $c = 41.2146(5)$ Å	$a = b = 7.14040(10)$ Å; $c = 25.1675(5)$ Å	$a = b = 7.08960(10)$ Å; $c = 25.4317(5)$ Å
Volume (Å^3)	1848.57(4)	1111.26(3)	1107.00(3)
Z	3	3	3
$D_{calc.}$ (g·cm^{-3})	3.0587	3.4157	3.4692
Data collection			
Diffractometer	Synchrotron	Synchrotron	Synchrotron
Radiation type	0.70848	0.70848	0.70848
λ (Å)	SLS, X06DA, PRIGo	SLS, X06DA, PRIGo	SLS, X06DA, PRIGo
Detector	Pilatus 2M-F	Pilatus 2M-F	Pilatus 2M-F
Time (sec.) / step size (°)	0.1 / 0.1	0.1 / 0.1	0.1 / 0.1
Number of frames	3600	3600	3600
θ range (°)	2.96–34.64	2.42–34.50	2.39–34.68
Index ranges	$-11 \le h \le 11$; $-9 \le k \le 9$; $-65 \le l \le 65$	$-10 \le h \le 10$; $-11 \le k \le 11$; $-39 \le l \le 40$	$-11 \le h \le 11$; $-10 \le k \le 10$; $-40 \le l \le 40$
No. of measured reflections	8246	6362	4861
No. of unique reflections	1036	608	618
Refinement of the structure			
No. of parameters	57	39	35
R_{int}	0.0368	0.1246	0.0393
R_1 (obs.) / R_1 (all)	0.0197 / 0.0216	0.0309 / 0.0334	0.0188 / 0.0217
wR_2(obs.) / wR_2 (all)	0.0271 / 0.0279	0.0360 / 0.0364	0.0227 / 0.0231
GOF (obs.) / GOF (all)	1.64 / 1.68	1.68 / 1.78	1.25 / 1.31
Δρ max / Δρ min [e Å^{-3}]	0.66 / −0.36	1.16 / −1.41	0.45 / −0.43

https://doi.org/10.1180/mgm.2022.103 Published online by Cambridge University Press

Table 2. The chemical composition of arctite-supergroup minerals from the Bellerberg volcano.*

	Nabimusaite			Gazeevite			Zadovite		
Constituent	Mean *n* = 15	S.D.	Range	Mean *n* = 11	S.D.	Range	Mean *n* = 9	S.D.	Range
SO_3	14.11	0.16	13.81–14.39	17.96	1.35	15.63–19.82	3.67	0.60	2.60–4.44
P_2O_5	0.27	0.06	0.17–0.39	1.56	0.54	0.63–2.25	20.32	1.06	19.30–22.32
V_2O_5	n.d.	–	–	0.22	0.11	0.05–0.43	1.19	0.18	0.83–1.44
SiO_2	19.87	0.30	19.33–20.35	15.99	0.43	15.55–16.99	10.15	0.55	9.08–10.79
TiO_2	0.17	0.11	0.01–0.35	n.d.	–	–	n.d.	–	–
Al_2O_3	0.42	0.21	0.11–0.74	0.09	0.02	0.07–0.13	n.d.	–	–
Fe_2O_3	0.17	0.10	0.01–0.33	0.16	0.11	0.03–0.37	0.12	0.06	0.01–0.20
CaO	58.53	0.23	58.16–59.10	44.40	0.35	43.86–45.21	43.13	0.34	42.59–43.56
SrO	0.94	0.22	0.62–1.22	0.70	0.11	0.58–0.91	0.37	0.07	0.25–0.50
BaO	0.29	0.45	0.00–1.19	17.33	0.42	16.84–18.09	19.53	0.16	19.31–19.74
Na_2O	0.16	0.05	0.10–0.27	0.13	0.08	0.02–0.32	0.21	0.11	0.07–0.42
K_2O	3.24	0.34	2.73–3.65	0.32	0.17	0.12–0.59	n.d.	–	–
F	1.54	0.11	1.32–1.71	0.84	0.15	0.64–1.04	2.49	0.07	2.31–2.56
–O=F	0.65			0.35			1.05		
Total	99.06			99.35			100.13		
Calculated on	27(O+F)			17(O+F)			17(O+F)		
Ca^{2+}	0.04			0.04			–		
Sr^{2+}	0.10			0.05			0.03		
Ba^{2+}	0.02			0.86			0.99		
K^{+}	0.79			0.05			–		
Sum A	0.95			1.00			1.02		
Ca^{2+}	11.94			6.00			5.96		
Na^{+}	0.06			0.03			0.05		
Sum B	12.00			6.03			6.01		
S^{6+}	0.06			–			–		
P^{5+}	–			–			0.69		
Si^{4+}	3.80			1.97			1.31		
Ti^{4+}	0.02			–			–		
Al^{3+}	0.10			0.02			–		
Fe^{3+}	0.02			0.01			–		
Sum T1	4.00			2.00			2.00		
S^{6+}	1.96			1.71			0.36		
P^{5+}	0.04			0.17			1.53		
V^{5+}	–			0.02			0.10		
Si^{4+}	–			0.06			–		
Fe^{3+}	–			–			0.01		
Sum T2	2.00			1.96			2.00		
F^{-}	0.93			0.34			1.01		
O^{2-}	0.07			0.53			–		
Sum W	1.00			0.87			1.01		

*S.D. = 1σ standard deviation; *n* – number of analyses; n.d. – not detected

refined at this site. S/P occupies the *T*2 site in gazeevite. Due to the similar scattering factors, the refinement of S and P has not been performed. However, the substitution of S for P was revealed in chemical analyses (~0.2 apfu of P^{5+}). In the *T*2 tetrahedron, there are three shorter *T*2–O3 = 1.476(4) Å and one longer *T*2–O4 = 1.499(4) Å bonds. Due to rotation, the BaO_6 octahedron could be linked to six equivalent *T*2-tetrahedra with the triangular base O3–O3–O3 (Fig. 5b). However, the O3 atom is half occupied, implying that, on average, only three *T*2-tetrahedra are linked to the BaO_6 octahedron. According to the EMPA, the emerged uncharged balance at the *T*2 site was balanced by F^{-} at the O5 site in the gazeevite structure due to the $S^{6+} + O^{2-} \leftrightarrow P^{5+} + F^{-}$ substitution scheme.

In the antiperovskite layers of gazeevite, the octahedron is centred by an $(O5)^{2-}$ anion coordinated by six Ca1 atoms, with the Ca1–O5 bond length equal to 2.4472(7) Å (Fig. 5c). The *T*1 $(SiO_4)^{4-}$ tetrahedra are placed between them. The Si atom is surrounded by three O2 in the base and one apical O1 atom with distances of 1.618(2) Å and 1.634(4) Å Si–O, respectively.

In the zadovite structure, similar to that of gazeevite, the polyhedral sites in the tetrahedral layers are occupied by Ba, enclosed by six PO_4 tetrahedra ascribed to the *T*2 site (Fig. 5e). The average Ba–O bond lengths (6 × Ba–O2 and 6 × Ba–O3) equal 3.3239 Å and 2.8012 Å, respectively. The average 1.539 Å P–O distance is nearly ideal for PO_4-tetrahedra, which does not confirm the chemical calculation and partial S substitution at this site. The antiperovskite layers in zadovite consist of regular FCa_6 octahedra with a F–Ca bond length of 2.5848(4) Å and tetrahedra at the *T*1 sites occupied by Si and P (Fig. 5f). The Si/P atoms at the *T*1 site bond three times to O2 = 1.588(12) Å and one slightly longer O1 = 1.604(3) Å, yielding the average 1.592 Å T1–O bond length.

Raman spectroscopy data

The Raman spectra of the arctite-supergroup minerals from xenoliths of the Bellerberg volcano are characterised by several fundamental bands in the 800–1200 cm^{-1} spectral range (Fig. 6). These bands are assigned to the symmetric (ν_1) and asymmetric (ν_3)

https://doi.org/10.1180/mgm.2022.103 Published online by Cambridge University Press

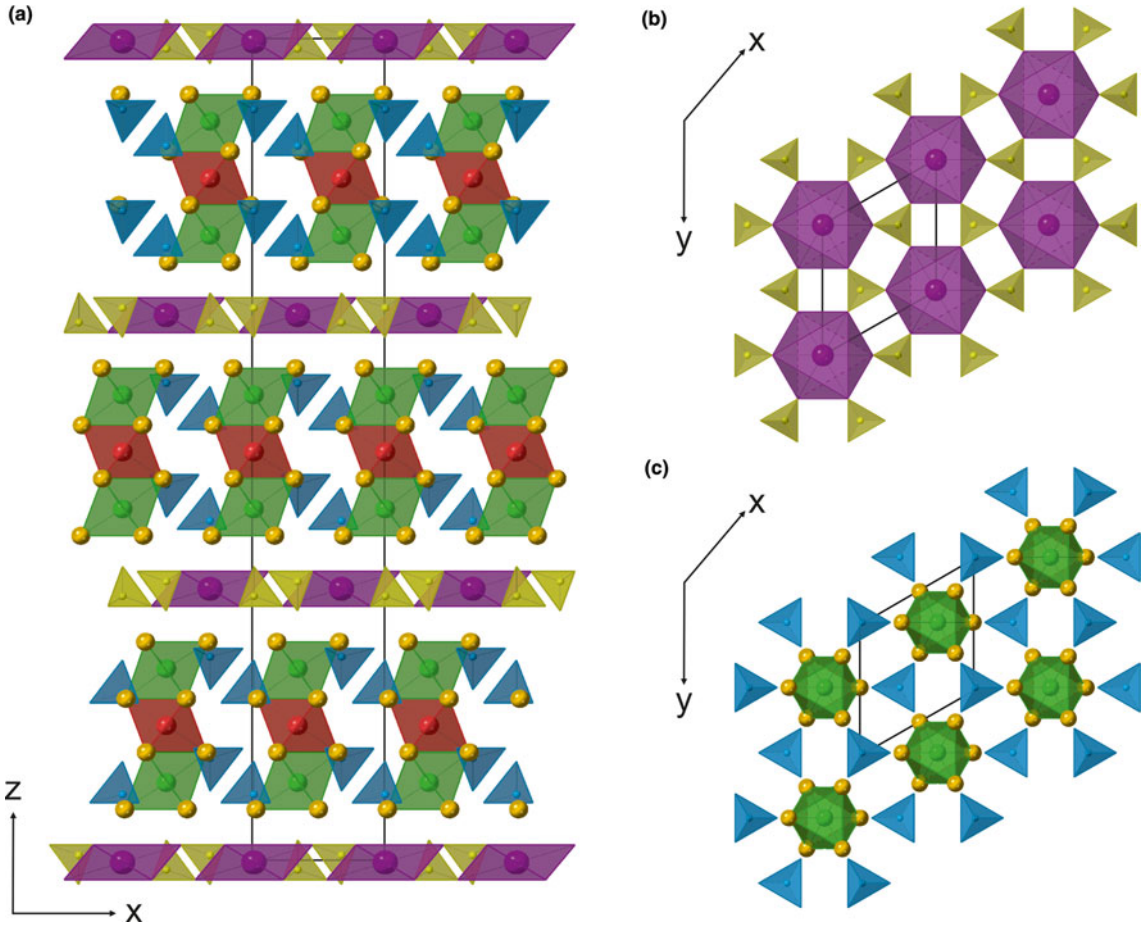

Fig. 4. The crystal structure of nabimusaite composed of single tetrahedral and triple antiperovskite layers (a). The K-octahedra (purple) are connected to the six SO_4-tetrahedra (yellow) within the tetrahedral layers (b). The linear face-sharing triplets of anion-centred FCa_6 (green) and OCa_6-octahedra (red) coordinated by Ca atoms (dark yellow spheres) (a) and surrounded by SiO_4-tetrahedra (blue) in an up and down sequence (c).

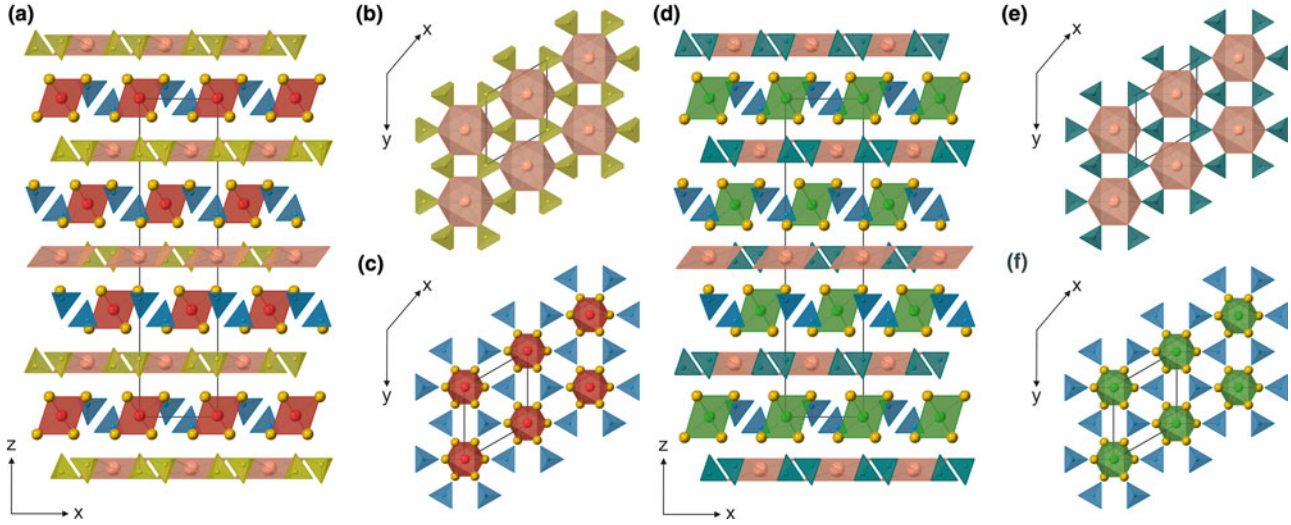

Fig. 5. The crystal structure of the zadovite type represented by gazeevite (a) and zadovite (d), characterised by the alternation of single tetrahedral (b,e) and single antiperovskite layers (c,f) along (001). The Ba-octahedra (pink) on T layers are surrounded by SO_4-tetrahedra (yellow) and PO_4-tetrahedra (sea-green) in the gazeevite (b) and zadovite (e) structure, respectively. The antiperovskite layers (A) are centred by O^{2-} (red) in the gazeevite structure (c) and by F^- (green) in the zadovite structure (f). Anion-centred octahedra are coordinated by Ca atoms (dark yellow spheres) and surrounded by six SiO_4-tetrahedra in gazeevite and SiO_4/PO_4-tetrahedra in zadovite (both in blue).

https://doi.org/10.1180/mgm.2022.103 Published online by Cambridge University Press

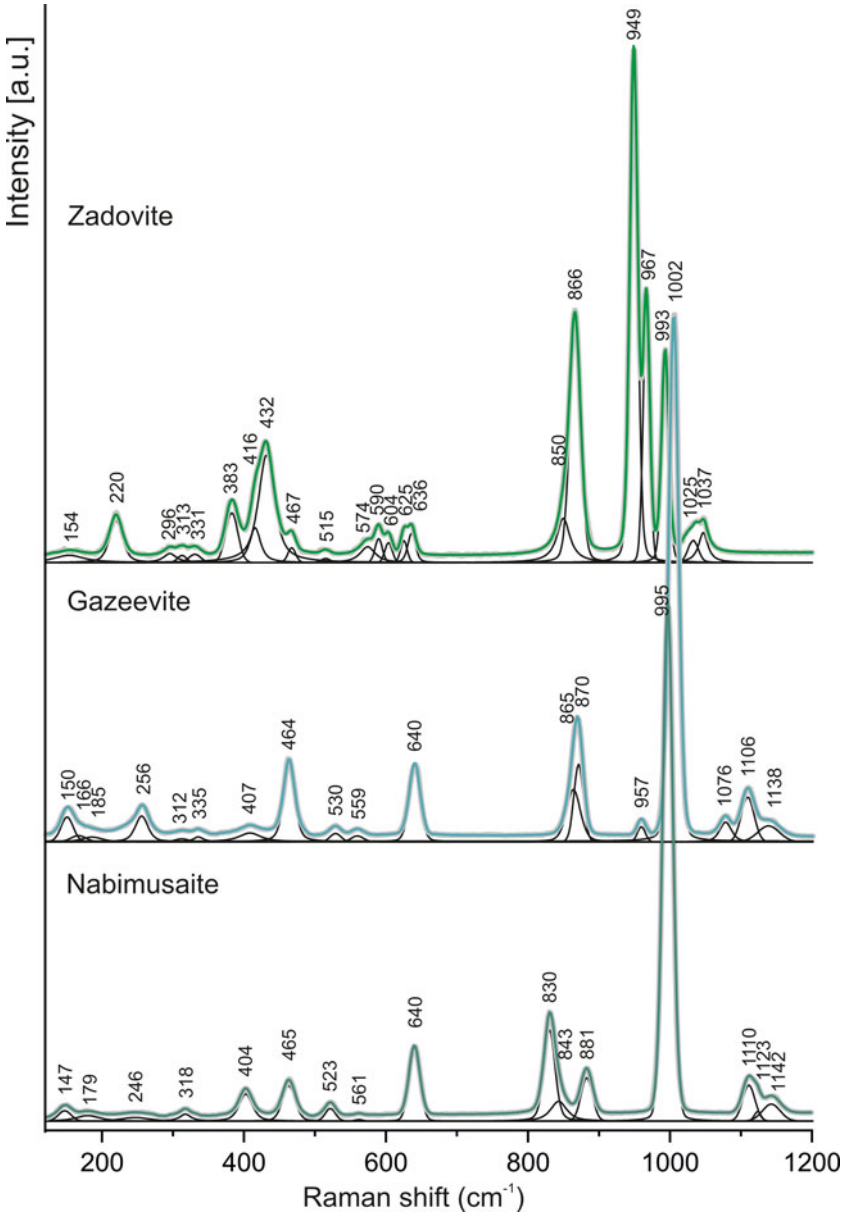

Fig. 6. The Raman spectra of nabimusaite, gazeevite and zadovite from the xenoliths of the Bellerberg volcano.

Table 3. A comparison of Raman band assignments for nabimusaite, gazeevite and zadovite from the Bellerberg volcano in Germany and the Hatrurim Complex in Israel.

Nabimusaite		Gazeevite		Zadovite		
This work	Galuskin *et al.* (2015a)	This work	Galuskin *et al.* (2017)	This work	Galuskin *et al.* (2015b)	Band assignments
147, 179	129	150, 166, 185	160	154	-	lattice vibrations
246	–	256	213, 266	220	222	K–O/Ba–O/Ca–O vibrations
318	–	312, 335	315	296, 313, 331	299	$R(TO_4)$, $T(TO_4)$
–	–	–	–	–	342	$\nu_2\ (VO_4)^{3-}$
404	403	407	413	383	389	$\nu_2\ (SiO_4)^{4-}$
–	–	–	–	416, 432	430	$\nu_2\ (PO_4)^{3-}$
465	463	464	468	467	–	$\nu_2\ (SO_4)^{2-}$
523, 561	524, 563	530, 559	529	515	520	$\nu_4\ (SiO_4)^{4-}$
–	–	–	560	574, 590, 604	589	$\nu_4\ (PO_4)^{3-}$
640	637	640	638	625, 636	627	$\nu_4\ (SO_4)^{2-}$
–	–	–	–	–	839	$\nu_1\ (VO_4)^{3-}$
830, 843, 881	831, 849, 885	865, 870	870	850, 866	865, 881	$\nu_1\ (SiO_4)^{4-}$
–	930, 948	957	963	949, 967	949,969	$\nu_1\ (PO_4)^{3-}$ / $\nu_3\ (SiO_4)^{4-}$
995	993	1002	1000	993	992	$\nu_1\ (SO_4)^{2-}$
–	–	–	–	1025, 1037	1031	$\nu_3\ (PO_4)^{3-}$
1110, 1123, 1142	1121	1076, 1106, 1138	1099, 1135	–	–	$\nu_3\ (SO_4)^{2-}$

https://doi.org/10.1180/mgm.2022.103 Published online by Cambridge University Press

stretching modes related to the (TO_4) tetrahedral group vibrations. The EMPA results confirm that the vibrations of the $(SiO_4)^{4-}$, $(SO_4)^{2-}$ and $(PO_4)^{3-}$ groups should be dominant in the Raman spectra of analysed mineral phases.

In the Raman spectrum of nabimusaite and gazeevite (Fig. 6), the most intense bands at 993 cm^{-1} and 1002 cm^{-1} are ascribed to the ν_1 symmetric stretching vibrations of the sulfate group, which occupy the *T*2 tetrahedral sites in the structure. The asymmetric ν_3 stretching modes of $(SO_4)^{2-}$ are observed in spectral ranges 1110–1145 cm^{-1} and 1075–1140 cm^{-1} for nabimusaite and gazeevite, respectively. In the Raman spectrum of zadovite, due to the substitution of S^{6+} at the *T*2 site confirmed by EMPA (Table 2), the band related to ν_1 $(SO_4)^{2-}$ appears at 993 cm^{-1}, with intensity relatively lower in comparison to this band intensity in two other spectra (Fig. 6). The zadovite spectrum is characterised by splitting the most intense band in the range ~950–970 cm^{-1} (Fig. 6). These two bands are related to the symmetric stretching vibrations of a $(PO4)^{3-}$ group and indicated that the phosphorus occupied two different *T* sites in the crystal structure. This fact was also reported in a previous publication and proved that the band at 949 cm^{-1} is assigned to the *T*2 site, whereas the band at 967 cm^{-1} is assigned to the *T*1 site, according to the site occupation and Raman spectra of the zadovite–aradite mineral series (Galuskin *et al.*, 2015b). Moreover, bands attributed to the ν_3 of $(SiO_4)^{4-}$ group, not observed in the zadovite spectrum, may overlap with the ν_1 $(PO_4)^{3-}$ vibrations in this spectral region. The band near ~1030 cm^{-1} with the relatively large full width at half maximum (FWHM) is ascribed to the asymmetric stretching vibrations of $(PO_4)^{3-}$. A more detailed fitting analysis allows dividing this band into two components placed at 1025 and 1037 cm^{-1}, indicating they assign the $(PO_4)^{3-}$ vibrations to two different tetrahedra. Low intense Raman bands ascribed to the symmetric stretching $(PO_4)^{3-}$ vibrations placed at 957 cm^{-1} in the gazeevite spectrum may be related to a noticeable P (0.17 apfu) content in its chemical composition.

The remaining Raman bands in this spectral range correspond to the symmetric stretching vibrations of the $(SiO_4)^{4-}$ group detected in each of the three presented spectra (Fig. 6). In the case of zadovite and gazeevite, in which the structure is featured by a single antiperovskite layer, the Raman band related to ν_1 $(SiO_4)^{4-}$ appears at ~870 cm^{-1} with shoulders at 850 and 865 cm^{-1}, respectively. Due to the presence of two symmetry-independent Si sites within the triple antiperovskite layer in the nabimusaite structure, the doubling of the Raman lines assigned to the ν_1 $(SiO_4)^{4-}$ vibrations are observed (Fig. 6). Bands related to this mode type occur at 830 cm^{-1} with low intense shoulders at 843 cm^{-1} and ~880 cm^{-1}.

The spectral range between 350 and 650 cm^{-1} is attributed to the symmetric (ν_2) and asymmetric (ν_4) bending modes associated with the vibrations of (TO_4) groups. The Raman spectra of nabimusaite and gazeevite in this region are similar and characterised by single bands at ~465 and 640 cm^{-1} assigned to the symmetric and asymmetric bending modes of $(SO_4)^{2-}$, respectively. Moreover, the Raman band at ~405 cm^{-1} with two low intense bands in the range ~525–560 cm^{-1} are related to the bending vibrations of $(SiO_4)^{4-}$ groups. In zadovite, bands associated with the modes of sulfate and silicate bending vibrations are also in similar spectral ranges. The Raman bands with wavenumber 467 cm^{-1} and at 625–636 cm^{-1} correspond to the ν_2 and ν_4 bending modes of $(SO_4)^{2-}$ group, whereas bands at 383 and 515 cm^{-1} correspond to the same vibrations of the $(SiO_4)^{4-}$ group. In addition, the zadovite spectrum is featured by a broad and intense band at 432 cm^{-1} with a shoulder at 416 cm^{-1}, which is connected to the symmetric bending vibrations of the $(PO_4)^{3-}$ groups, while asymmetric bending modes are observed as a few low intense bands in the range ~575–605 cm^{-1} (Fig. 6).

In the Raman spectra (Fig. 6), several bands in the range 280–330 cm^{-1} are ascribed to the rotational and translational modes of (TO_4) groups. The single Raman bands at 246 cm^{-1} in nabimusaite, 256 cm^{-1} in gazeevite, and 220 cm^{-1} in zadovite are related to the K–O, Ba–O and Ca–O stretching vibrations, respectively. Mentioned bands belong to the lattice acoustic modes and may also occur in the low wavenumber region below 200 cm^{-1}.

Discussion

The individual analysis of holotype nabimusaite discovered in the Jabel Harmun locality (Hatrurim Complex, West Bank) indicated enrichment of Ba, up to as much as ~5.0 wt.% BaO (Galuskin *et al.*, 2015a). In turn, the highest K_2O content is equal to 3.65 wt.%. For the average chemical composition of the holotype nabimusaite, the ratio of these two components is ~27% to 63% for Ba^{2+} and K^+, respectively. These results indicated the significant involvement of the $BaCa_{12}(SiO_4)_4(SO_4)_2O_3$ end-member, known as dargaite (Galuskina *et al.*, 2019), in a complex solid-solution represented by the holotype nabimusaite. In the case of the German counterpart, the polyhedral site is 83% occupied by K^+, whereas the Ba^{2+} contents are a negligible amount, ~2% in accordance with chemical results. In addition, the notable contribution of ~11% Sr^{2+} is also observed (Table 2). For the tetrahedral sites, the presence of additional impurities does not exceed 0.2 and 0.4 apfu in nabimusaite from Bellerberg and Jabel Harmun localities, respectively.

The holotype gazeevite described from the Shadil-Khokh volcano and a few outcrops of pyrometamorphic rocks of the Hatrurim Complex is characterised by similar compositions (Galuskin *et al.*, 2017). Approximated results were also obtained for the gazeevite detected in the carbonate–silicate xenolith from Bellerberg volcano, Germany. In both cases, the differentiated substitution of S^{6+} for P^{5+} at the *T*2 position in tetrahedral layers is observed. The presence of P^{5+} at this site implies the occurrence of F^- in the OCa_6 anion-centred octahedron, which compensates charge balance due to the $S^{6+} + O^{2-} \leftrightarrow P/V^{5+} + F^-$ scheme.

The main difference between the data obtained and the holotype zadovite was observed primarily in the V^{5+} content that is six-times higher (0.65 apfu) in the holotype sample than in the zadovite from Germany (0.10 apfu). The authors of the holotype material description confirm that the significant variations in the chemical composition are caused by the occurrence of the zadovite–aradite series in the pyrometamorphic rocks of the Hatrurim Complex (Galuskin *et al.*, 2015b). Based on their results, the V_2O_5 content in zadovite was never lower than 2–3 wt.%. However, the chemical analyses performed for zadovite, detected in paralava from Zuk Tamrur locality (Hatrurim Complex, Israel), confirm lower V_2O_5 contents ~1.15 wt.% (Krzątała *et al.*, 2020), which is approximate to the values obtained for zadovite reported in Caspar quarry (Table 2). Moreover, in both specimens, due to the $Si^{4+}+S^{6+}\leftrightarrow 2P^{5+}$ substitution scheme at the tetrahedral sites, variations of these element content are observed.

The results obtained with the single-crystal X-ray diffraction in this work are in good agreement with the structural data for the holotype nabimusaite, gazeevite and zadovite (Galuskin *et al.*, 2015a, 2015b, 2017). The minor differences appear in the site population and bond lengths between atoms, mostly in tetrahedra, caused by the difference in composition. However, in the

https://doi.org/10.1180/mgm.2022.103 Published online by Cambridge University Press

previous description of the nabimusaite structure, fluorine (corresponding to the O8 site) was incorporated into the central antiperovskite layer, and the refinement was performed in analogy to the synthetic $KCa_{12}(SiO_4)_4(SO_4)_2O_2F$ phase (Fayos *et al.*, 1985; Galuskin *et al.*, 2015a). The subsequent BVS (bond-valence sums) calculation revealed that instead of being internal, F occupied the external antiperovskite layers related to the $O7Ca_6$ octahedra (Galuskina *et al.*, 2019). Therefore, the original model for natural and synthetic nabimusaite is not entirely correct and should be revised. The present paper has demonstrated the correct refinement for nabimusaite from the Bellerberg volcano. The anion-centred octahedra in the internal antiperovskite layer are occupied by O^{2-} (O8), whereas F^- (O7) is located in the external layers together with O^{2-} in a ratio of 50/50.

Unlike the holotype specimen, gazeevite described here does not show the splitting of oxygen atoms on O3 and O3A and the rotational disorder of SO_4-tetrahedra of ca. ± 6° around [001] within the tetrahedral layers. In the previous description, this effect was explained by the various occupancies of the Ba site by Ba^{2+} (81%) and a considerable amount of K^+ (19%) and their differences in charges and ionic radii (Galuskin *et al.*, 2017). Nevertheless, gazeevite from the Caspar quarry xenolith revealed a much lower K occupation (8%) at the Ba site, which did not cause deformations in the structure.

The Raman spectra for arctite-supergroup minerals from the Bellerberg volcano are very similar to the spectra of the holotype species (Galuskin *et al.*, 2015a; 2015b, 2017) and are compared in Table 3. Minor differences in the number of bands and their intensity are related to the random crystal orientation during the measurements and some variability in the chemical composition. In the case of nabimusaite spectra from both localities, differences are indistinguishable (Table 3). The same observations were made for gazeevite spectra. However, we consider that band at 560 cm^{-1} in the holotype gazeevite is more probably related to the symmetric bending vibrations of $(SiO_4)^{4-}$ than $(VO_4)^{3-}$, as was proposed before (Galuskin *et al.*, 2017). The higher SO_3 content observed in German zadovite made it possible to also distinguish, in addition to the bands attributed to stretching vibrations, bands related to the (ν_2) symmetric bending vibration of $(SO_4)^{2-}$ at 467 cm^{-1}, which was not detected in the Raman spectrum of the holotype zadovite. In contrast, due to the higher V_2O_5 content in the holotype zadovite, Raman bands at 839 and 342 cm^{-1} are assigned to the symmetric stretching and bending vibrations of $(VO_4)^{3-}$, respectively (Table 3). The results suggest that minerals belonging to the arctite supergroup might be easily identified by Raman spectroscopy.

The Hatrurim Complex located in Israel, Jordan and some territories of Palestine (West Bank), is a large geological unit composed of high-temperature low-pressure pyrometamorphic rocks (Bentor *et al.*, 1963; Gross, 1977; Burg *et al.*, 1991; Geller *et al.*, 2012; Novikov *et al.*, 2013). The most common are clinker-like pyrometamorphic rocks (spurrite marbles, larnite pseudoconglomerates, gehlenite hornfelses) and various paralavas (Bentor *et al.*, 1963; Sokol *et al.*, 2007; Vapnik *et al.*, 2007; Grapes, 2010; Galuskina *et al.*, 2014). Previous research focusing on minerals of the arctite supergroup has shown that nabimusaite and gazeevite were found in larnite–ye'elimite nodules of pyrometamorphic rocks known as pseudoconglomerates, featured by the presence of visible microfractures and increased porosity (Galuskin *et al.*, 2015a, 2017), whereas zadovite was usually detected within the rankinite paralava hosted by gehlenite hornfelses (Galuskin *et al.*, 2015b; Krzątała *et al.*, 2020). Gazeevite was also recognised in an altered carbonate–silicate xenolith embedded in rhyodacite lava on the northwest slope of the Shadil-Khokh volcano (Galuskin *et al.*, 2017). According to mineral paragenesis and temperature conditions, it was reported that the formation of nabimusaite and gazeevite in the Hatrurim Complex is combined with high-temperature alteration of primary mineral assemblages, mainly fluorellestadite and larnite, affected by K- and Ba-enriched sulfate melt generated probably by the combustion processes (Galuskin *et al.*, 2015a, 2017). In addition, the occurrence of gazeevite in xenoliths of the Shadil-Khokh volcano might be connected with the presence of sulfate-enriched intergranular melt (Galuskin *et al.*, 2017). In turn, the formation of zadovite in small enclaves within the paralava of the Hatrurim Complex is an effect of residual melt crystallisation enriched in incompatible elements such as Ba, V, P, U, S, Ti and Nb, formed after relatively fast crystallisation of the main constituents of paralava (Galuskin *et al.*, 2015b; Galuskina *et al.*, 2017; Krzątała *et al.*, 2020).

We conclude that nabimusaite and gazeevite from Germany probably formed during a similar crystallisation scheme described above. High-temperature clinker-like phases such as larnite, ternesite and fluorellestadite detected in xenoliths were altered and reacted later with sulfate-bearing melt, leading to nabimusaite and gazeevite crystallisation. Moreover, the presence of jasmundite in association with nabimusaite may indicate that the reaction of altered primary phases occurs not only in the presence of melt but also with some volatile components transported by different gases generated by volcanic activity. In turn, xenomorphic zadovite grains identified in a xenolith sample from the Bellerberg volcano between wollastonite, gehlenite and alumoåkermanite crystals, together with other Ba-minerals (bennesherite, fresnoite, walstromite and celsian) formed after them, due to reactions of Ba concentrated in the intergranular spaces filled with a liquid phase, most probably melt with silica composition enriched in Na, as well as Al, Ti and Al.

Minerals of the arctite supergroup are very rare and have been described from only a few localities to date, most of which belong to the Hatrurim Complex (Galuskin *et al.*, 2021). In addition to pyrometamorphic rocks and xenoliths from the Shadil-Khokh volcano, the Bellerberg volcano is now another locality where more than one member of this supergroup was detected. As was noted, usually, these mineral phases occur as an accessory, however, some might be distinguished as rock-forming minerals, such as the nabimusaite described herein or the aravaite identified in some spurrite rock of the Hatrurim Complex (Galuskin *et al.*, 2021). The difference between the analysed samples and previous reports is related to the co-occurrence of the arctite-supergroup minerals within each rock sample. In three analysed xenolith samples from the Bellerberg volcano, nabimusaite, gazeevite and zadovite occur separately, whereas, in rocks of the pyrometamorphic Hatrurim Complex, the solid solution of zadovite–aradite (Galuskin *et al.*, 2015b), nabimusaite–dargaite (Galuskina *et al.*, 2019), or nabimusaite, dargaite, gazeevite (Galuskin *et al.*, 2017) and ariegilatite–stracherite (Galuskin *et al.*, 2018a) associations within one rock specimen were reported. Further investigation of carbonate–silicate xenoliths from the Bellerberg volcano area in Germany could potentially allow for similar observations and identification of other members of the arctite supergroup.

Acknowledgements. We thank Hannes Krüger (University of Innsbruck) for significant technical assistance during the diffraction experiments at X06DA and three anonymous reviewers for their helpful and constructive comments, which allowed us to improve a previous version of the manuscript.

https://doi.org/10.1180/mgm.2022.103 Published online by Cambridge University Press

Supplementary material. To view supplementary material for this article, please visit https://doi.org/10.1180/mgm.2022.103

Competing interests. The authors declare none.

References

Abraham K., Gebert W., Medenbach O., Schreyer W. and Hentschel G. (1983) Eifelite, $KNa_3Mg_4Si_{12}O_{30}$, a new mineral of the osumilite group with octahedral sodium. *Contributions to Mineralogy and Petrology*, **82**, 252–258.

Bentor Y.K., Gross S. and Heller L. (1963) Some unusual minerals from the "Mottled Zone" complex, Israel. *American Mineralogist*, **48**, 924–930.

Burg A., Starinsky A., Bartov Y. and Kolodny Y. (1991) Geology of the Hatrurim Formation (Mottled Zone) in the Hatrurim basin. *Israel Journal of Earth Sciences*, **40**, 107–124.

Chukanov N.V., Britvin S.N., Van K.V., Möckel S. and Zadov A.E. (2012) Kottenheimite, $Ca_3Si(SO_4)_2(OH)_6{\cdot}12H_2O$, a new ettringite-group mineral from the Eifel area, Germany. *The Canadian Mineralogist*, **50**, 55–63.

Chukanov N.V., Aksenov S.M., Rastsvetaeva R.K., Blass G., Varlamov D.A., Pekov I.V., Belakovskiy D.I. and Gurzhiy V.V. (2015) Calcinaksite, $KNaCa(Si_4O_{10}){\cdot}H_2O$, a new mineral from the Eifel volcanic area, Germany. *Mineralogy and Petrology*, **109**, 397–404.

Fayos J., Glasser F.P., Howie R.A., Lachowski E. and Perez-Mendez M. (1985) Structure of dodecacalcium potassium fluoride dioxide tetrasilicate bis(sulphate), $KF.2[Ca_6(SO_4)(SiO_4)_2O]$: a fluorine-containing phase encountered in cement clinker production process. *Acta Crystallographica*, **C41**, 814–816.

Galuskin E.V., Gfeller F., Armbruster T., Galuskina I.O., Vapnik Y., Murashko M., Włodyka R. and Dzierżanowski P. (2015a) New minerals with a modular structure derived from hatrurite from the pyrometamorphic Hatrurim Complex. Part I. Nabimusaite, $KCa_{12}(SiO_4)_4(SO_4)_2O_2F$, from larnite rocks of Jabel Harmun, Palestinian Autonomy, Israel. *Mineralogical Magazine*, **79**, 1061–1072.

Galuskin E.V., Gfeller F., Galuskina I.O., Pakhomova A., Armbruster T., Vapnik Y., Włodyka R., Dzierżanowski P. and Murashko M. (2015b) New minerals with a modular structure derived from hatrurite from the pyrometamorphic Hatrurim Complex. Part II. Zadovite, $BaCa_6[(SiO_4)(PO_4)](PO_4)_2F$ and aradite, $BaCa_6[(SiO_4)(VO_4)](VO_4)_2F$, from paralavas of the Hatrurim Basin, Negev Desert, Israel. *Mineralogical Magazine*, **79**, 1073–1087.

Galuskin E.V., Krüger B., Krüger H., Blass G., Widmer R. and Galuskina I.O. (2016) Wernerkrauseite, $CaFe^{3+}_2Mn^{4+}O_6$: the first nonstoichiometric post-spinel mineral, from Bellerberg volcano, Eifel, Germany. *European Journal of Mineralogy*, **28**, 485–493.

Galuskin E.V., Gfeller F., Galuskina I.O., Armbruster T., Krzątała A., Vapnik Y., Kusz J., Dulski M., Gardocki M., Gurbanov A.G. and Dzierżanowski P. (2017) New minerals with a modular structure derived from hatrurite from the pyrometamorphic rocks. Part III. Gazeevite, $BaCa_6(SiO_4)_2(SO_4)_2O$, from Israel and the Palestine Autonomy, South Levant, and from South Ossetia, Greater Caucasus. *Mineralogical Magazine*, **81**, 499–513.

Galuskin E.V., Krüger B., Galuskina I.O., Krüger H., Vapnik Y., Wojdyla J.A. and Murashko M. (2018a) New Mineral with Modular Structure Derived from Hatrurite from the Pyrometamorphic Rocks of the Hatrurim Complex: Ariegilatite, $BaCa_{12}(SiO_4)_4(PO_4)_2F_2O$, from Negev Desert, Israel. *Minerals*, **8**, 109.

Galuskin E.V., Krüger B., Galuskina I.O., Krüger H., Vapnik Y., Pauluhn A. and Olieric V. (2018b) Stracherite, $BaCa_6(SiO_4)_2[(PO_4)(CO_3)]F$, the first CO_3-bearing intercalated hexagonal antiperovskite from Negev Desert, Israel. *American Mineralogist*, **103**, 1699–1706.

Galuskin E., Galuskina I., Krüger B., KrügeR H., Vapnik Y., Krzątała A., Środek D. and Zieliński G. (2021) Nomenclature and Classification of the Arctite Supergroup. Aravaite, $Ba_2Ca_{18}(SiO_4)_6[(PO_4)_3(CO_3)]F_3O$, a New Arctite Supergroup Mineral from Negev Desert, Israel. *The Canadian Mineralogist*, **59**, 191–209.

Galuskina I.O., Vapnik Y., Lazic B., Armbruster T., Murashko M. and Galuskin E.V. (2014) Harmunite $CaFe_2O_4$: A new mineral from the Jabel Harmun, West Bank, Palestinian Autonomy, Israel. *American Mineralogist*, **99**, 965–975.

Galuskina I.O., Galuskin E.V., Vapnik Y., Prusik K., Stasiak M., Dzierżanowski P. and Murashko M. (2017) Gurimite, $Ba_3(VO_4)_2$ and hexacelsian, $BaAl_2Si_2O_8$ – two new minerals from schorlomite-rich paralava of the Hatrurim Complex, Negev Desert, Israel. *Mineralogical Magazine*, **81**, 1009–1019.

Galuskina I.O., Gfeller F., Galuskin E.V., Armbruster T., Vapnik Y., Dulski M., Gardocki M., Jeżak L. and Murashko M. (2019) New minerals with modular structure derived from hatrurite from the pyrometamorphic rocks. Part IV: Dargaite, $BaCa_{12}(SiO_4)_4(SO_4)_2O_3$, from Nahal Darga, Palestinian Autonomy. *Mineralogical Magazine*, **83**, 81–88.

Geller Y.I., Burg A., Halicz L. and Kolodny Y. (2012) System closure during the combustion metamorphic "Mottled Zone" event, Israel. *Chemical Geology*, **344**, 25–36.

Grapes R. (2010) *Pyrometamorphism*. 2nd ed., Springer, Berlin-Heidelberg.

Gross S. (1977) The mineralogy of the Hatrurim Formation, Israel. *Geological Survey of Israel Bulletin*, **70**, 80 pp.

Hentschel G. (1987) *Die Mineralien der Eifelvulkane*. 2nd ed., Weise Verlag, München, Germany.

Irran E., Tillmanns E. and Hentschel G. (1997) Ternesite, $Ca_5(SiO_4)_2SO_4$, a new mineral from the Ettringer Bellerberg/Eifel, Germany. *Mineralogy and Petrology*, **60**, 121–132.

Juroszek R., Krüger H., Galuskina I., Krüger B., Jeżak L., Ternes B., Wojdyla J., Krzykawski T., Pautov L. and Galuskin E. (2018) Sharyginite, $Ca_3TiFe_2O_8$, a new mineral from the Bellerberg Volcano, Germany. *Minerals*, **8**, 308.

Khomyakov A.P., Bykova A.V. and Kurova T.A. (1983) Arctite, $Na_2Ca_4(PO_4)_3F$, a new mineral. *International Geology Review*, **25**, 739–740.

Krüger B., Krüger H., Galuskin E.V., Galuskina I.O., Vapnik Y., Olieric V. and Pauluhn A. (2018) Aravaite, $Ba^2Ca^{18}(SiO^4)^6(PO^4)^3(CO^3)F^3O$: modular structure and disorder of a new mineral with single and triple antiperovskite layers. *Acta Crystallographica*, **B74**, 492–501.

Krzątała A., Krüger B., Galuskina I., Vapnik Y. and Galuskin E. (2020) Walstromite, $BaCa_2(Si_3O_9)$, from Rankinite Paralava within Gehlenite Hornfels of the Hatrurim Basin, Negev Desert, Israel. *Minerals*, **10**, 407.

Mihajlovic T., Lengauer C.L., Ntaflos T., Kolitsch U. and Tillmanns E. (2004) Two new minerals rondorfite, $Ca_8Mg[SiO_4]_4Cl_2$, and almarudite, $K(\square,Na)_2(Mn,Fe,Mg)_2(Be,Al)_3[Si_{12}O_{30}]$, and a study of iron-rich wadalite, $Ca_{12}[(Al_8Si_4Fe_2)O_{32}]Cl_6$, from the Bellerberg (Bellberg) volcano, Eifel, Germany. *Neues Jahrbuch für Mineralogie - Abhandlungen*, 265–294.

Novikov I., Vapnik Y. and Safonova I. (2013) Mud volcano origin of the Mottled Zone, South Levant. *Geoscience Frontiers*, **4**, 597–619.

Petříček V., Dušek M. and Palatinus L. (2014). Crystallographic Computing System JANA2006: General features, *Zeitschrift für Kristallographie*, **229**, 345–352.

Sokol E.V., Novikov I.S., Vapnik Ye. and Sharygin V.V. (2007) Gas fire from mud volcanoes as a trigger for the appearance of high-temperature pyrometamorphic rocks of the Hatrurim Formation (Dead Sea area). *Doklady Earth Sciences*, **413**, 474–480.

Sokol E.V., Kokh S.N., Seryotkin Y.V., Deviatiiarova A.S., Goryainov S.V., Sharygin V.V., Khoury H.N., Karmanov N.S., Danilovsky V.A. and Artemyev D.A. (2020) Ultrahigh-temperature sphalerite from Zn-Cd-Se-rich combustion metamorphic marbles, Daba Complex, Central Jordan: paragenesis, chemistry, and structure. *Minerals*, **10**, 822.

Sokolova E.V., Yamnova N.A., Egorov-Tismenko Y.K. and Khomyakov A.P. (1984) Crystal structure of arctite, a new sodium calcium barium phosphate $(Na_5Ca)Ca_6Ba[PO_4]_6F_3$. *Proceedings of the USSR Academy of Sciences*, **274**, 78–83.

Vapnik Y., Sharygin V.V., Sokol E.V. and Shagam R. (2007) Paralavas in a combustion metamorphic complex: Hatrurim Basin, Israel. *GSA Reviews in Engineering Geology*, **18**, 133–153.

https://doi.org/10.1180/mgm.2022.103 Published online by Cambridge University Press